

# Primary Object Segmentation in Aerial Videos via Hierarchical Temporal Slicing and Co-Segmentation

Pengcheng Yuan<sup>1</sup>, Jia Li<sup>1,2\*</sup>, Daxin Gu<sup>1</sup>, Yonghong Tian<sup>3,4</sup>

<sup>1</sup>State Key Laboratory of Virtual Reality Technology and Systems, SCSE, Beihang University

<sup>2</sup>International Research Institute for Multidisciplinary Science, Beihang University

<sup>3</sup>School of Electronics Engineering and Computer Science, Peking University

<sup>4</sup>Cooperative Medianet Innovation Center, China

## ABSTRACT

Primary object segmentation plays an important role in understanding videos generated by unmanned aerial vehicles. In this paper, we propose a large-scale dataset **APD** with 500 aerial videos, in which the primary objects are manually annotated on 5,014 sparsely sampled frames. To the best of our knowledge, it is the largest dataset to date for the task of primary object segmentation in aerial videos. From this dataset, we find that most aerial videos contain large-scale scenes, small sized primary objects as well as consistently varying scales and viewpoints. Inspired by that, we propose a novel hierarchical temporal slicing approach that repeatedly divides a video into two sub-videos formed by the odd and even frames, respectively. In this manner, an aerial video can be represented by a set of hierarchically organized short video clips, and the primary objects they share can be segmented by training end-to-end co-segmentation CNNs and finally refined within the neighborhood reversible flows. Experimental results show that our approach remarkably outperforms 24 state-of-the-art methods in segmenting primary objects in various types of aerial videos.

## KEYWORDS

Primary object segmentation, unmanned aerial vehicles, video co-segmentation, CNNs

## 1 INTRODUCTION

Recently, unmanned aerial vehicles (drones) have become very popular since it provides a new way to observe and explore the world. As a result, aerial videos generated by drones have been growing explosively. For these videos, one of the key tasks is to segment the primary objects, which can be used to facilitate subsequent tasks such as event understanding [31], scene reconstruction [23], drone navigation [44] and visual tracking [5].

Hundreds of models have been proposed in the past decade to segment primary objects, which can be roughly divided into two categories. The first category contains image-based models that focus on detecting salient (primary) objects in images. In this category, classic models such as [7, 34, 43] focus on designing rules to pop-out salient targets and suppress distractors, while recent models [6, 9, 21, 35] usually adopt the deep learning framework due to the availability of large-scale image datasets like DUT-OMRON [41], MSRA-B [1, 12, 22] and XPIE [39]. The second category contains video-based models that aim to segment a sequence of primary/foreground objects that consistently pop-out in the whole video. Similar to the image-based category, classic video-based models

\*Corresponding author: Jia Li (E-mail: jiali@buaa.edu.cn)

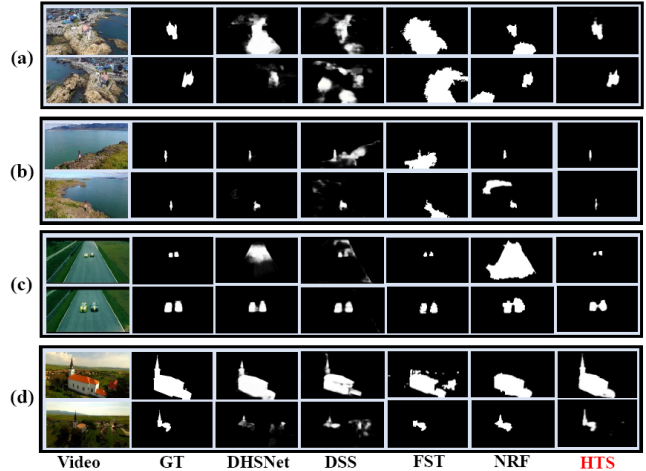


**Figure 1: Representative challenging scenarios in aerial videos.** Frames and ground-truth (GT) masks are taken from our dataset APD that cover challenging cases of (a) large-scale scenes, (b) small-sized primary objects, (c) scale variation, (d) viewpoint variation. We also demonstrate the results of state-of-the-art image-based and video-based models for salient/primary object segmentation, including DHSNet [21], DSS [9], FST [25], NRF [19] and our HTS approach.

such as [25, 29, 37, 38] also design rules to segment primary objects by jointly considering the per-frame accuracy and inter-frame consistency. Recently, with the presence of large-scale video datasets like VOS [18] and DAVIS [27], several deep learning models have been proposed as well. For example, Li *et al.* [19] adopted complementary CNNs to initialize per-frame predictions of primary objects, which were then refined along neighborhood reversible flows that reflected the most reliable temporal correspondences between far-away frames. Caelles *et al.* [4] proposed a semi-supervised video object segmentation approach that adopted CNNs to transfer generic semantic information to the task of foreground segmentation. In [18], saliency-guided stacked autoencoders were adopted to encode multiple saliency cues into spatiotemporal saliency scores for video object segmentation. In addition, some video object co-segmentation [8, 42] have been proposed as well to simultaneously segment a common category of objects from two or more videos. For example, Fu *et al.* [8] proposed a co-selection graph to formulate correspondences between different videos, and extended this framework to handle multiple objects using a multi-state selection graph model.

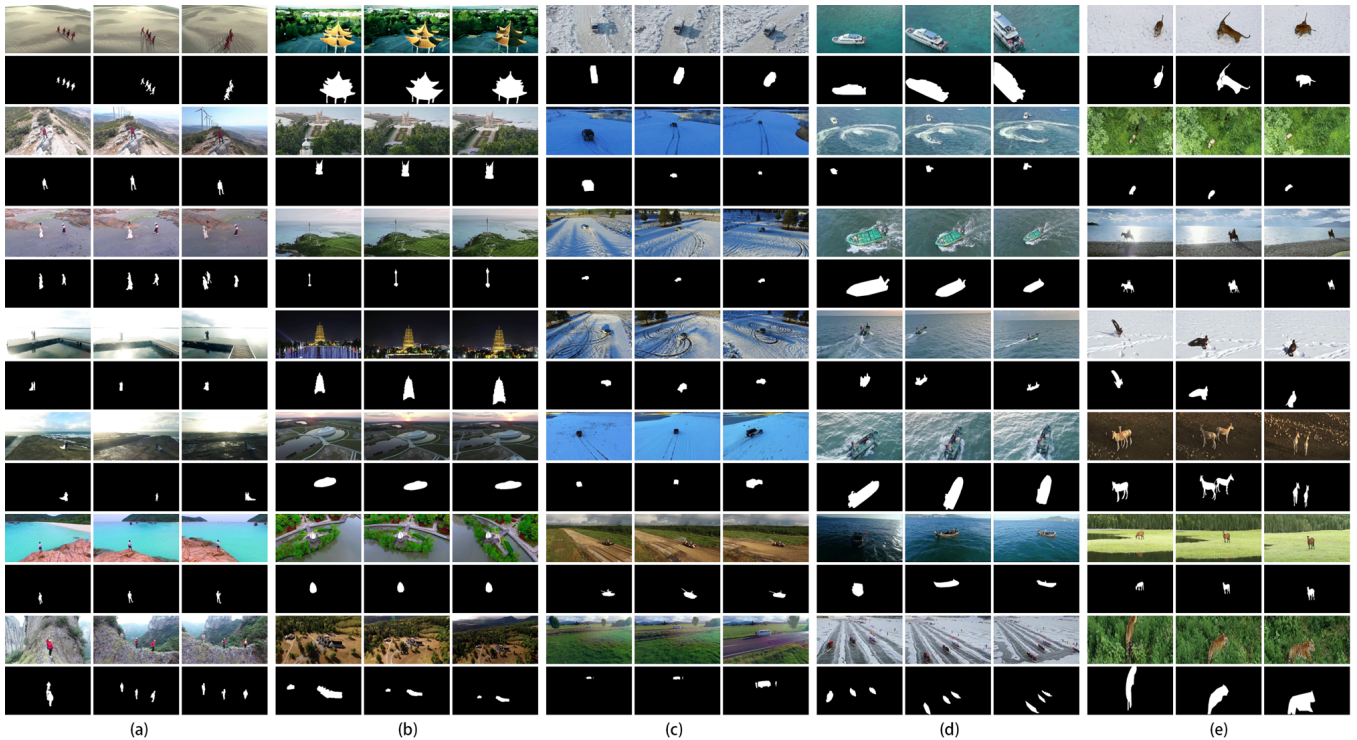


**Figure 2: Representative video frames from the APD and their ground-truth masks of primary objects. The 500 videos in APD are divided into five categories according to the types of primary objects they contains, including (a) APD-Human (95 videos), (b) APD-Building (121 videos), (c) APD-Vehicle (56 videos), (d) APD-Boat (180 videos) and (e) APD-Other (48 videos).**

Generally speaking, most existing models from the two categories can perform impressively on generic images and videos taken on the ground. However, their capability in processing aerial videos, which often contain large-scale scenes, small sized primary objects as well as consistently varying scales and viewpoints, may be not very satisfactory (see Fig. 1 for some representative examples). The main reasons are two-folds: 1) the heuristic rules and learning frameworks may not perfectly fit the characteristics of aerial videos, and 2) there is a lack of large-scale aerial video datasets for model training and benchmarking. Toward this end, this paper proposes a large-scale dataset **APD** with 500 aerial videos (76,221 frames). Based on the types of primary objects, these videos can be divided into five subsets, including humans, buildings, vehicles, boats and others. From these videos, 5,014 frames are sparsely sampled, in which the primary objects are manually annotated (see Fig. 2 for representative frames and their ground-truth masks).

Based on the aerial video dataset **APD**, we propose a hierarchical temporal slicing approach for primary object segmentation in aerial videos. We first divide a long aerial video into two sub-videos formed by the odd and even frames, respectively. By repeatedly conducting such temporal slicing operations to the sub-videos, a long video can be represented by a set of hierarchically organized sub-videos. As a result, the object segmentation problem in a long aerial video can be resolved by co-segmenting the objects shared by much shorter sub-videos. By learning end-to-end CNNs for co-segmenting two frames, a mask can be initialized for each frame by co-segmenting frames

from sub-videos that have the same parent node in the hierarchy. These masks are then refined within the neighborhood reversible flows so that the primary video objects can consistently pop-out in the video. Extensive experimental results on the proposed aerial dataset as well as a generic video dataset show that our approach is efficient and outperforms 24 state-of-the-art models, including 11 image-based non-deep models, 8 image-based deep models and 5 video-based models. The results also show that **APD** is a very challenging dataset for existing object segmentation models.

The contributions of this work are summarized as follows: 1) we propose a dataset for primary object segmentation in aerial videos, which, to the best of our knowledge, is currently the largest one. This dataset can be used to further investigate the problem of primary video object segmentation from a completely new perspective; 2) we propose a hierarchical temporal slicing framework that can efficiently and accurately segment primary objects in aerial videos with co-segmentation CNNs; and 3) we provide a benchmark of our approach and massive state-of-the-art models on the proposed dataset, and such benchmarking results can be re-used by subsequent works to facilitate the development of new models.

## 2 APD: A DATASET FOR PRIMARY OBJECT SEGMENTATION IN AERIAL VIDEO

Towards primary object segmentation in aerial videos, we construct a large scale video dataset for model training and benchmarking,

**Table 1: Comparison between our dataset and another six generic video object segmentation datasets. #Annot: the number of annotated frames; #MaxF and #MinF: the max and min numbers of frames in a video; #Avg-Obj: the average number of objects per video; Avg-Area: the average area of primary objects per video.**

Dataset	#Video	Max Res.	#Frames	#MaxF	#MinF	#Annot	#Avg-Obj	Avg-Area (%)
SegTrack [33]	6	414 × 352	244	71	21	244	1.00 ± 0.00	3.46 ± 2.84
SegTrack V2 [16]	14	640 × 360	1,065	279	21	1,065	1.38 ± 1.01	7.38 ± 7.89
FBMS [3]	50	960 × 540	13,860	800	19	720	1.78 ± 1.54	14.4 ± 13.7
DAVIS [27]	90	1920 × 1080	3,455	104	25	3,455	5.39 ± 22.9	8.10 ± 6.44
ViSal [38]	17	512 × 288	963	100	30	193	1.16 ± 0.40	10.5 ± 6.51
VOS [18]	200	800 × 800	116,103	2,249	71	7,467	1.15 ± 0.44	13.0 ± 12.6
<b>APD-Human</b>	95	720 × 1280	14,638	271	61	966	1.40 ± 0.64	1.50 ± 0.07
<b>APD-Building</b>	121	720 × 1280	17,749	271	31	1,170	1.16 ± 0.20	7.17 ± 0.57
<b>APD-Vehicle</b>	56	720 × 1280	7,665	280	31	505	1.14 ± 0.14	2.54 ± 0.09
<b>APD-Boat</b>	180	720 × 1280	28,085	280	16	1,851	1.27 ± 0.31	3.52 ± 0.32
<b>APD-Other</b>	48	720 × 1280	8,084	284	86	522	1.45 ± 0.58	2.80 ± 0.09
<b>APD</b>	500	720 × 1280	76,221	284	16	5,014	1.27 ± 0.36	3.86 ± 0.33

denoted as **APD**. The construction process and dataset statistics are described as follows.

**Dataset Construction.** In constructing the dataset, we first collect 2,402 long aerial videos (107 hours in total) shared on the Internet. After that, we manually divide long videos into 52,712 shots and remove shots that are unlikely to be taken by drones or contain no obvious primary objects (determined through voting by three volunteers). After that, we obtain 21,395 video clips, from which we randomly sample 500 clips for the subsequent annotation process (76,221 frames in total). According to the types of primary objects, these videos are further divided into five subsets, including humans (95 videos), buildings (121 videos), vehicles (56 videos), boats (180 videos) and others (48 videos). From these videos, we uniformly sample only one keyframe out of every 15 frames and manually annotate the 5,090 keyframes.

The annotation process is conducted by three annotators with the LabelMe toolbox [30]. In the annotation process, each annotator is requested to first watch the videos to obtain an initial impression of what are the primary video objects. Based on the impression, they then annotate the primary objects in the sparsely sampled keyframes with polygons. After that, the annotation quality of each frame is then independently assessed by another two subjects. Flawed annotations are then corrected by the three annotators through majority voting, while frames with confusing annotations are discarded. Finally, we obtain 5,014 binary masks that indicate the location of primary video objects in keyframes.

**Dataset Statistics.** To demonstrate the major characteristics of **APD**, we show the detailed statistics of **APD** and its five subsets in Table 1. In addition, to facilitate the comparison between **APD** and previous datasets, we also show the information of six representative video datasets with massive ground-based videos for primary semantic/salient object segmentation, including SegTrack [33], SegTrack V2 [16], FBMS [3], DAVIS [27], ViSal [38] and VOS [18].

As shown in Table 1, the primary objects in **APD** are remarkably smaller than that in most previous datasets (except SegTrack, which is a small dataset with only one object annotated per frame). Such small sized objects will make the segmentation task of primary

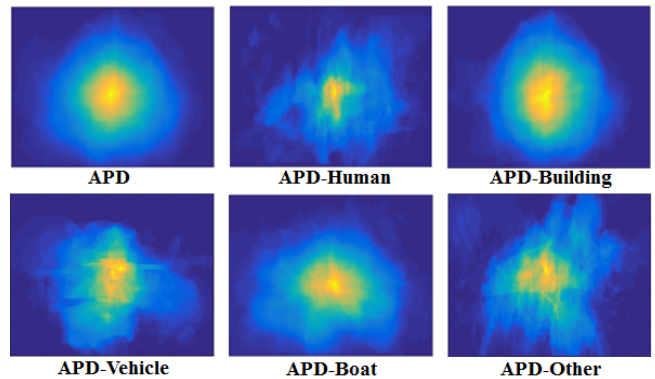


**Figure 3: Average annotation maps of APD and its subsets.**

objects very difficult. In particular, in the categories of humans and vehicles, the primary objects are even smaller than the other three categories. Considering that there already exist many ground-based approaches for the detection, segmentation and recognition of humans and vehicles, the **APD** dataset provides an opportunity to find out a way that can transfer ground-based knowledge of humans and vehicles to aerial videos. Moreover, the number of videos in **APD** are larger than most previous datasets, and all these videos are from five clearly defined object categories. In this sense, it is possible to directly train video-based deep learning models on **APD** with less risk of over-fitting.

Beyond the quantitative statistics, we also show the average annotation maps of **APD** and its subsets in Fig. 3. As stated in [18], an average annotation map is computed by resizing all annotated masks to the same resolution, summing them pixel by pixel, and normalizing the cumulative map to a maximum value of 1. From Fig. 3, we find that the distribution of primary objects also have a strong center-bias tendency, implying that many rules and models for generic primary/salient object segmentation can be re-used for segmenting primary objects in aerial videos (*e.g.*, the boundary prior [43]). Moreover, the degrees of center-bias in the five subsets



differ from each other, indicating that there may exist several different ways to optimally segment primary objects in aerial videos if their semantic attributes are known or predictable.

### 3 A HIERARCHICAL TEMPORAL SLICING APPROACH FOR PRIMARY OBJECT SEGMENTATION IN AERIAL VIDEOS

The challenges of large-scale scenes, small-sized objects and consistently varying scales and viewpoints make the segmentation task of primary objects in aerial videos very challenging. Fortunately, we find that most primary objects last for a long period in the majority of aerial video sequences, which may be caused by the fact that aerial videos usually have less or slower camera motion. Inspired by this fact, we propose a novel approach to address the problem of primary video object segmentation in aerial videos by turning a complex task to several simple ones. The framework of our approach is shown in Fig. 4, which consists of three major stages: 1) hierarchical temporal slicing of aerial videos, 2) mask initialization via video object co-segmentation and 3) mask refinement within neighborhood reversible flows. Details of these three stages are described as follows.

#### 3.1 Stage 1: Hierarchical Temporal Slicing of Aerial Videos

In the first stage, we divide a long aerial video into two sub-videos formed by the odd and even frames, respectively. In this manner, the content similarity between the two sub-videos can be maximally guaranteed. By repeatedly conducting such temporal slicing operations to all sub-videos, a hierarchy of short video clips can be efficiently constructed. Assuming that primary objects last for at least  $N$  frames in an aerial video, we can build a tree structure with a depth of  $\lfloor \log_2^N \rfloor$  and  $2^{\lfloor \log_2^N \rfloor}$  nodes. Here we empirically set  $N = \max(32, \text{video length})$ . The short video clips at each leaf node has at least one frame that contains the primary objects. As a result, primary objects in the original video can be segmented by solving a set of simpler tasks: co-segmenting the objects shared by massive much shorter video clips.

#### 3.2 Stage 2: Mask Initialization via Video Object Co-segmentation

In the second stage, we aim to initialize a mask of primary objects for each video frame by co-segmenting the objects shared by the  $2^{\lfloor \log_2^N \rfloor}$  short video clips at leaf nodes. To speed up this process, the co-segmentation is conducted only between two sub-videos that have the same parent node. Let  $\mathbb{A} = \{A_i, i = 1, \dots, |\mathbb{A}|\}$  and  $\mathbb{B} = \{B_j, j = 1, \dots, |\mathbb{B}|\}$  be two short video clips, where  $|\mathbb{A}|$  and  $|\mathbb{B}|$  denote the numbers of frames in  $\mathbb{A}$  and  $\mathbb{B}$ , respectively. For these two short videos, we assume that there exists a model  $\phi(A_i, B_j)$  that can segment the objects shared by the  $i$ th frame of  $\mathbb{A}$  and the  $j$ th frame of  $\mathbb{B}$ :

$$\phi(A_i, B_j) = \{M_{A_i|B_j}, M_{B_j|A_i}\}, \quad (1)$$

where  $M_{A_i|B_j}$  is a probability map for the frame  $A_i$  that depicts the objects it shares with the frame  $B_j$ . By co-segmenting all frame pairs between  $\mathbb{A}$  and  $\mathbb{B}$ , the mask of primary objects for a frame  $A_i$  can be initialized as the per-pixel average of all such co-segmentation

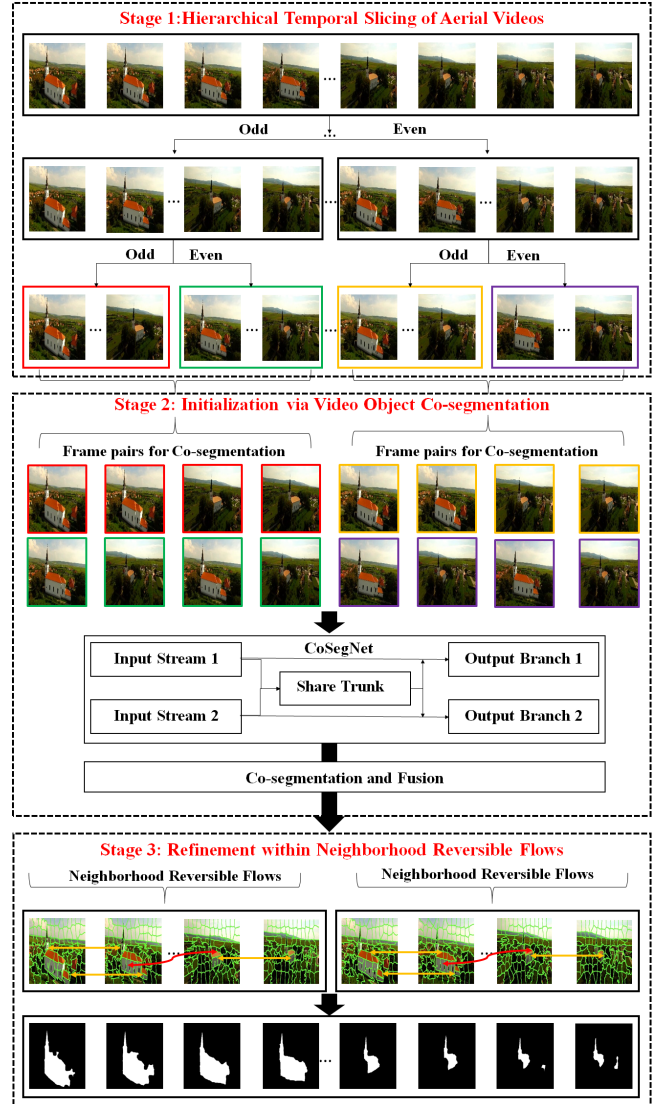


Figure 4: Framework of our approach. In this framework, videos are first hierarchically divided into much shorter video clips, which are then co-segmented to initialize per-frame masks. Primary objects are then segmented via mask refinement within neighborhood reversible flows.

results with respect to all frames from  $\mathbb{B}$ :

$$M_{A_i} = \frac{1}{|\mathbb{B}|} \sum_{j=1}^{|\mathbb{B}|} M_{A_i|B_j}. \quad (2)$$

For the probability map produced by (2), we can see that each frame is actually co-segmented with multiple non-adjacent frames with increasing temporal distances. The advantages of such co-segmentation between far-away frames are at least four-folds: First, far-away frames can provide more useful cues of the primary objects in the co-segmentation process than adjacent frames that are full of redundant visual stimuli. In other words, far-away frames



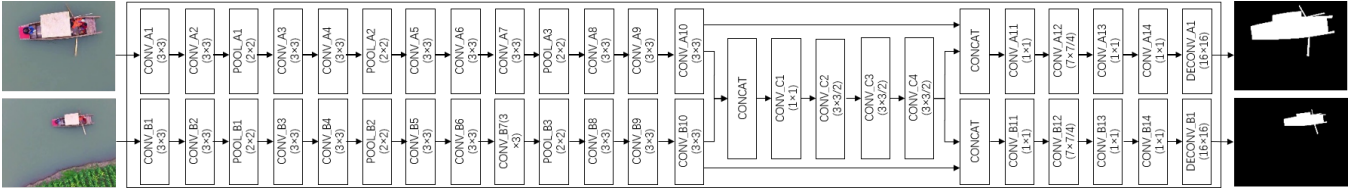


Figure 5: The network architecture of CoSegNet. The symbol  $a \times a/b$  indicates kernel size  $a$  and dilation parameter  $b$ .

form a global picture of what is the primary video object. Second, most co-segmentation operations can pop-out primary objects since they appear in a large portion of video frames. Thus the primary objects can be repeatedly enhanced through the additive fusion in (2). Third, the hierarchical framework ensures that each frame can be co-segmented with at least one frame with the same primary objects. Last but not least, the computational cost of co-segmenting frame pairs from two short videos is remarkably smaller than that from two long videos so that the efficiency of the proposed approach can be improved.

In practice, the model  $\phi(A_i, B_j)$  can be set to any co-segmentation algorithms. In this study, we simply train two-stream fully convolutional neural networks, denoted as CoSegNet, to justify the effectiveness of the proposed hierarchical temporal slicing and co-segmentation framework. As shown in Fig. 5, CoSegNet takes two frames as the input and two probability maps as the output. Features from the two frames are extracted with two separate branches, which are initialized with the architecture and parameters of the first several layers of VGG16 [32]. After that, the output feature maps of these two streams are concatenated and fused into a shared trunk for extracting the common features of the two frames. Then the network splits into two separate branches that predict a probability map of shared objects for each input frame. Note that a skip connection from each input stream is also incorporated to the corresponding output branch so as to regularize the generation of each probability map by introducing frame-specific low-level features.

In training CoSegNet, we sample pairs of annotated frames from the training set of APD. For a pair of frames  $I_i$  and  $I_j$  with ground-truth binary masks  $G_i$  and  $G_j$ , we train CoSegNet by minimizing two losses  $l(M_{I_i|I_j}, G_i)$  and  $l(M_{I_j|I_i}, G_j)$ , where  $l(\cdot)$  is the cross-entropy loss. We resize all input frames and output predictions to the resolution of  $320 \times 320$ . The learning rate is set to  $2 \times 10^{-6}$  at the first 50000 iterations and  $2 \times 10^{-7}$  in subsequent iterations. The Caffe platform [10] is adopted in training the network with a batch size of 8 frame pairs. The optimization algorithm is set to Adam, the gamma is set to 0.1 and the momentum is set to 0.9.

### 3.3 Stage 3: Mask Refinement within Neighborhood Reversible Flows

After co-segmenting two short videos A and B, each video frame obtains an initial object mask represented by a probability map. Recall that the videos A and B under the same parent node are generated by the odd and even frames of a longer sub-video  $\mathbb{C} = \{C_1, C_2, \dots, C_{|\mathbb{C}|}\}$ , we assume that each frame  $C_u$  is initialized with a probability maps  $M_{C_u}$ .

To enhance inter-frame consistency and correct probable errors in  $M_{C_u}$ , a key challenge is to derive reliable inter-frame correspondences. Considering that frames in the sub-video  $\mathbb{C}$  may be actually far away from each other in the original video, the pixel-based optical flow may fail to handle large pixel displacement. To address this problem, we construct neighborhood reversible flows [19] based on superpixels. We first apply the SLIC algorithm [2] to divide two frames  $C_u$  and  $C_v$  into  $N_u$  and  $N_v$  superpixels that are denoted as  $\{O_{ui}\}$  and  $\{O_{vj}\}$ , respectively. Similar to [19], we compute the pair-wise  $\ell_1$  distances between superpixels from  $\{O_{ui}\}$  and  $\{O_{vj}\}$ , where a superpixel is represented by its average RGB, Lab and HSV colors as well as the horizontal and vertical positions. Suppose that  $O_{ui}$  and  $O_{vj}$  reside in the  $k$  nearest neighbors of each other, they are  $k$ -nearest neighborhood reversible with the correspondence measured by

$$f_{ui,vj} = \begin{cases} \exp(-2k/\sigma) & \text{if } k \leq \sigma \\ 0 & \text{otherwise} \end{cases} \quad (3)$$

where  $\sigma$  is a constant empirically set to 15 to suppress weak correspondence. Such superpixel-based inter-frame correspondence between  $C_u$  and  $C_v$  is denoted as the neighborhood reversible flow  $\mathbf{F}_{u,v} \in \mathbb{R}^{N_u \times N_v}$ , in which the component at  $(i, j)$  equals  $f_{ui,vj}$ . Note that we further normalize  $\mathbf{F}_{u,v}$  so that each row sums up to 1. Based on such flows, we refine the initial mask  $M_{C_u}$  according its correlations with other frames. To speed up the refinement, we only refer to the previous mask  $M_{C_{u-1}}$  and subsequent mask  $M_{C_{u+1}}$ . We first turn the pixel-based map  $M_{C_u}$  to a vectorized superpixel-based map  $\mathbf{x}_u$  by averaging the scores of all pixels inside each superpixel. After that, the score in  $\mathbf{x}_u$  is updated as

$$\hat{\mathbf{x}}_u = \frac{\mathbf{x}_u + \lambda_p \cdot \mathbf{F}_{u,u-1} \mathbf{x}_{u-1} + \lambda_s \cdot \mathbf{F}_{u,u+1} \mathbf{x}_{u+1}}{1 + \lambda_p + \lambda_s} \quad (4)$$

where  $\lambda_p$  and  $\lambda_s$  are two constants to balance the influence of previous and subsequent frames. In experiments, we set  $\lambda_p = \lambda_s = 0.5$ . After the temporal propagation, we turn superpixel-based scores into pixel-based ones as

$$\hat{M}_{C_u}(p) = \sum_{i=1}^{N_u} \delta(p \in O_{ui}) \cdot \hat{\mathbf{x}}_u \quad (5)$$

where  $\hat{M}_{C_u}$  is the refined probability map of  $C_u$  that depict the presence of primary objects.  $\delta(p \in O_{ui})$  is an indicator function which equals 1 if  $p \in O_{ui}$  and 0 otherwise. An adaptive threshold  $0.2 \cdot \max(\{\hat{M}_{C_u}(p), \forall p \in C_u\})$  is then used to segment the primary objects in the frame  $C_u$ .

**Table 2: Performance benchmark of our approach HTS and 24 state-of-the-art models on APD and its five subsets. The best and runner-up models of each column are marked with bold and underline, respectively.**

Models	APD-Human		APD-Building		APD-Vehicle		APD-Boat		APD-Other		APD		
	mIoU	wFM	mIoU	wFM	mIoU	wFM	mIoU	wFM	mIoU	wFM	mIoU	wFM	
[I+N]	CB [11]	.050	.101	.162	.260	.145	.265	.111	.183	.252	.448	.126	.228
	BSCA [28]	.044	.107	.186	.277	.177	.233	.120	.186	.222	.347	.131	.219
	DSR [20]	.149	.243	.250	.334	.219	.310	.232	.318	.327	.425	.222	.329
	RBD [46]	.162	.275	.232	.319	.257	.351	.275	.363	.373	.491	.243	.357
	SMD [26]	.244	.304	.240	.312	.306	.354	.329	.376	.416	.481	.294	.365
	GMR [41]	.138	.200	.211	.279	.250	.269	.193	.239	.315	.302	.202	.258
	GP [13]	.033	.053	.172	.238	.124	.169	.123	.174	.177	.243	.119	.177
	MB+ [43]	.115	.189	.219	.276	.241	.325	.247	.313	.315	.406	.220	.300
	HS [40]	.037	.091	.145	.273	.132	.210	.119	.186	.274	.398	.123	.218
	HDCT [14]	.137	.288	.241	.342	.234	.413	.249	.413	.314	.542	.221	.396
	ELE+ [39]	.268	.295	.330	.360	.425	.453	.411	.451	.521	.452	.371	.417
[I+D]	DCL [17]	.349	.433	.341	.394	.503	.566	.511	.554	.561	.583	.444	.515
	DHSNet [21]	.394	<u>.472</u>	.387	.438	.523	<u>.601</u>	<u>.572</u>	<u>.655</u>	.626	.701	.493	<u>.581</u>
	DSS [9]	.277	.409	.326	.389	.474	.564	.462	.572	.509	.668	.400	.517
	ELD [15]	.165	.247	.289	.353	.269	.326	.320	.417	.429	.521	.294	.389
	FSN [6]	.286	.324	.363	.393	.507	.554	.519	.580	.589	.664	.443	.505
	LEGS [35]	.064	.093	.260	.331	.225	.292	.172	.228	.334	.415	.193	.261
	MCDL [45]	.147	.049	.243	.138	.283	.147	.277	.141	.422	.155	.262	.129
	RFCN [36]	.338	.378	.360	.398	.467	.521	.521	.561	.603	.671	.451	.510
[V]	SSA [18]	.284	.348	.263	.331	.366	.432	.350	.421	.489	.551	.333	.414
	NRF [19]	.393	.433	<u>.423</u>	<u>.449</u>	.507	.540	.552	.598	<u>.677</u>	<u>.741</u>	<u>.496</u>	.551
	FST [25]	.272	.308	.190	.213	<u>.535</u>	.596	.342	.399	.375	.440	.319	.382
	MSG [8]	.080	.088	.160	.186	.216	.232	.143	.172	.361	.410	.153	.182
	RMC [42]	.123	.136	.202	.226	.312	.336	.208	.231	.230	.265	.205	.233
	HTS	<b>.485</b>	<b>.555</b>	<b>.533</b>	<b>.594</b>	<b>.700</b>	<b>.753</b>	<b>.678</b>	<b>.744</b>	<b>.696</b>	<b>.781</b>	<b>.617</b>	<b>.695</b>

## 4 EXPERIMENTS

In the experiments, we compare the proposed approach (denoted as HTS) with 24 state-of-the-art models on **APD** to demonstrate 1) the effectiveness of the proposed approach and dataset, and 2) the key challenges in aerial-based primary video object segmentation. The 24 models to be compared with can be divided into three groups:

1) The **[I+N]** group contains 11 image-based non-deep models, including CB [11], BSCA [28], DSR [20], RBD [46], SMD [26], GMR [41], GP [13], MB+ [43], HS [40] and HDCT [14].

2) The **[I+D]** group contains 8 image-based deep models, including DCL [17], DHSNet [21], DSS [9], ELD [15], FSN [6], LEGS[35], MCDL [45] and RFCN [36].

3) The **[V]** group contains 5 video-based models, including FST [25], SSA [18], NRF [19], MSG [8] and RMC [42]. Note that SSA and NRF also utilize deep learning components such as stacked autoencoders and CNNs, while MSG and RMC are video co-segmentation models.

In the comparisons, we divide **APD** into three subsets: 50% for training, 25% for validation and 25% for testing. On the testing subset with 125 videos, we evaluate the model performance with two metrics, including the mean Intersection-over-Union (mIoU) and the weighted F-Measure (wFM). The mIoU score is computed following the way proposed in [18], which first computes the IoU score at each frame and then step-wisely average them on each video

and the whole dataset to balance the influence of short and long videos. Note that the thresholds for turning probability maps into binary masks are set to 20% of the maximal probability scores, as suggested in [19]. Similarly, the wFM score is computed with the source code provided by [24] that assess the overall segmentation performance by jointly considering the completeness and exactness.

### 4.1 Comparison with State-of-the-art Models

The performance scores of HTS and the other 24 state-of-the-art models on **APD** and its five subsets (only the 125 testing videos) are shown in Table 2. In addition, we also illustrate the results of HTS on representative frames in Fig. 6.

From Table 2, we can see that HTS outperforms the other 24 models on the whole dataset and all the five subsets. We also find that **APD** is a very challenging dataset for most existing salient/primary object segmentation models. The image-based non-deep models perform far from satisfactory, especially on the **APD-Human** subset since the primary objects cover only 1.5% area of the video frames on average (see Table 1). Most image-based deep models outperform non-deep ones, indicating that the learned features are more robust than heuristic rules when the application scenarios are transferred from ground-based to aerial. In particular, among the image-based deep models, LEGS, MCDL and ELD have the worst overall performance, which may be caused by the fact that such models often rely

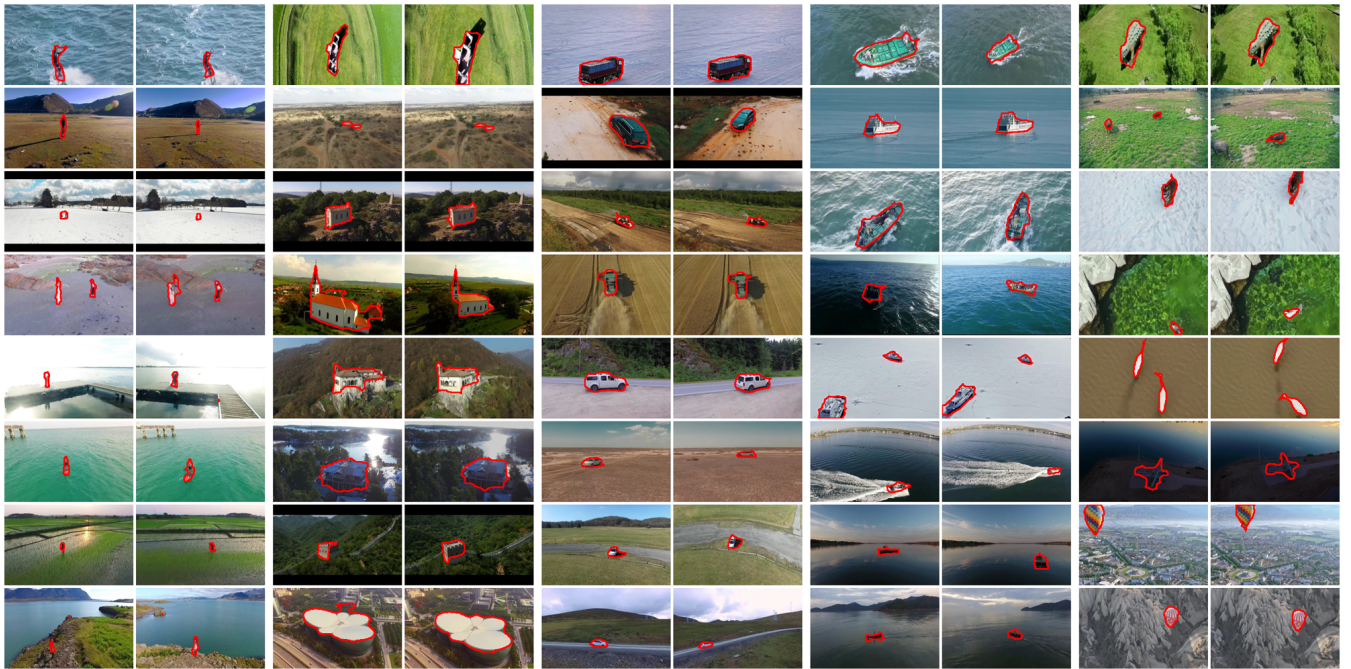


Figure 6: Results of our HTS approach on representative video frames from APD.

heavily on pre-segmented superpixels. For the small-sized primary objects such as humans and vehicles, the superpixels may be inaccurate for feature extraction. Moreover, among video-based models, NRF achieves impressive performance scores that are much higher than SSA and FST. This implies that the CNNs learned on generic image datasets can be partially reused in aerial videos, while the predictions can be further refined by using the inter-frame correspondences (*e.g.*, in NRF and HTS). Moreover, the performances of some models, such as NRF and DHSNet, have different ranks in terms of mIoU and wFM. This phenomena may imply that mIoU and wFM are two metrics that reveal the model performance from two different perspectives. Therefore, we suggest to use both metrics for model evaluation on APD.

Beyond the direct performance comparisons, we fine-tune three top-performed deep models, DSS, NRF and DHSNet, on the same APD videos used to train our HTS model and test the fine-tuned models again for a more fair comparison. As shown in Table 3, we find that HTS performs slightly better than the other three deep models fine-tuned on APD. This indicates that NRF, DSS and DHSNet, the state-of-the-art salient/primary object segmentation models, can learn some useful cues for primary object segmentation in aerial videos. However, in many aerial videos the primary objects are very small and thus not always salient in all frames. They are just consistently shared by the majority of video frames and keep on capturing human attention throughout the videos (*e.g.*, the buildings in Fig. 6). These results imply that the task of segmenting primary objects from a video is not equivalent to the task of separately segmenting salient objects from each frames. On the contrary, CoSegNet well resolves the problem from the perspective of co-segmentation. Even when the scene contains rich content and small-sized primary objects, the

Table 3: Model performance after being fine-tuned on APD.

Models	Before Fine-tuning		After Fine-tuning	
	mIoU	wFM	mIoU	wFM
DSS [9]	0.400	0.517	0.575	0.688
NRF [19]	0.496	0.551	0.609	0.687
DHSNet [21]	0.493	0.581	0.587	0.685
HTS	-	-	0.617	0.695

co-segmentation framework can enforce CoSegNet to learn the features from the objects shared by different frames, leading to higher performance than these deep models.

## 4.2 Detailed Performance Analysis

Beyond the comparisons with state-of-the-arts, we also conduct several experiments to provide an in-depth performance analysis from the perspective of effectiveness, generalization ability, computational complexity and framework rationality.

**Effectiveness test of odd-even temporal slicing.** To validate the effectiveness of the odd-even temporal slicing framework, we test HTS again by hierarchically dividing the testing videos into the same number of sub-videos formed by consecutive frames other than the even and odd frames. Note that the same HTS model pre-trained on the training set of APD is used for co-segmentation. In the case, the mIoU of HTS decreases from 0.617 to 0.608, and the wFM decreases from 0.695 to 0.689, implying the odd-even slicing framework provides better frame pairs for co-segmentation.



**Generalization ability test.** In order to validate HTS model is generic in various scenes, we test HTS over VOS [18], a dataset for primary object segmentation with mainly ground-based videos. On this dataset, we re-train and compare HTS with NRF, which is also previously fine-tuned to achieve its best performance on VOS. In the experiments, we equally divide the 200 videos of VOS into two subsets. By training HTS on one subset and test it on the other subset for two times, we obtain the segmentation results for all the 200 VOS videos. On the VOS dataset, our HTS model has mIoU of 0.717 and wFM of 0.771, which slightly outperforms NRF (mIoU=0.717 and wFM=0.765) on the ground-based videos from VOS. As a result, we can safely claim that HTS can be used as a generic framework that have the potential of segmenting primary objects in both aerial and ground-level videos.

**Complexity and rationality.** Another concern about the proposed approach may be the complexity and rationality of the hierarchical temporal slicing framework. Theoretically, a deeper hierarchy can speed up the co-segmentation process since CoSegNet will operate on all frame pairs formed by probable combinations of all frames from two sub-videos. However, a deeper hierarchy also leads to over-segmented videos, and a frame will be co-segmented with only far-away frames. To validate these two points, we conduct another experiment that divides the a testing video into the depth 2, 3, 4, 5 and 6. The performance scores and co-segmentation times can be found in Table 4. We can see that the experimental results will match the theoretical analysis: a deeper hierarchy leads to almost stable performance but remarkably lower computational complexity. Such results justify the rationality of using the hierarchical temporal slicing framework. In most experiments, we adopt a depth of 5, which corresponds to the assumption that a primary object will consistently appear for at least 32 frames (*i.e.*, about 1s). Considering that one co-segmentation operation in CoSegNet takes only 4ms on GPU (NVIDIA GTX 1080) and refinement via neighborhood reversible flow takes 1.32s on CPU, HTS takes 1.82s per frame when processing a video with 181 frames.

## 5 CONCLUSION

In this paper, we propose a large-scale dataset for primary object segmentation in aerial videos. The dataset consists of 500 videos from five semantic categories, which is currently the largest aerial video dataset in this area. We believe this dataset will be helpful for the development of video object segmentation techniques. Based on the dataset, we propose a hierarchical temporal slicing approach for primary video segmentation in aerial videos, which repeatedly divides a video into short sub-videos that are assumed to share the same primary objects. As a result, the original segmentation task is converted to a set of co-segmentation tasks, which are then resolved by training CNNs for co-segmenting frame pairs and being refined within neighborhood reversible flows. Experimental results show that the proposed dataset is very challenging and the proposed approach outperform 24 state-of-the-art models.

In the future work, we will try to explore the difference between the visual patterns extracted from ground-based and aerial videos so as to facilitate the design of better models for primary video object segmentation. In addition, the probability of constructing CNNs that can directly co-segment two short videos will be explored as well.

**Table 4: Performance and complexity of HTS when the 125 testing video are temporally sliced into different depth. #Co-Seg indicates the number of co-segmentation operations.**

Depth	mIoU	wFM	#Co-Seg
2	0.613	0.693	785K
3	0.614	0.693	379K
4	0.616	0.694	177K
5	0.617	0.695	76K
6	0.615	0.693	25K

## REFERENCES

- [1] R. Achanta, S. Hemami, F. Estrada, and S. Susstrunk. 2009. Frequency-tuned salient region detection. In *CVPR*.
- [2] R. Achanta, A. Shaji, K. Smith, A. Lucchi, P. Fua, and S. S. Susstrunk. 2012. SLIC Superpixels Compared to State-of-the-Art Superpixel Methods. *IEEE TPAMI* (2012).
- [3] Thomas Brox and Jitendra Malik. 2010. Object segmentation by long term analysis of point trajectories. In *ECCV*.
- [4] Sergi Caelles, Kevis-Kokitsi Maninis, Jordi Pont-Tuset, Laura Leal-Taixé, Daniel Cremers, and Luc Van Gool. 2017. One-shot video object segmentation. In *CVPR*.
- [5] D. Cavaliere, V. Loia, A. Saggese, S. Senatore, and M. Vento. 2017. Semantically Enhanced UAVs to Increase the Aerial Scene Understanding. *IEEE TSMC:Systems* (2017).
- [6] Xiaowu Chen, Anlin Zheng, Jia Li, and Feng Lu. 2017. Look, Perceive and Segment: Finding the Salient Objects in Images via Two-Stream Fixation-Semantic CNNs. In *ICCV*.
- [7] M. M. Cheng, N. J. Mitra, X. Huang, P. H. S. Torr, and S. M. Hu. 2015. Global Contrast Based Salient Region Detection. *IEEE TPAMI* (2015).
- [8] Huazhu Fu, Dong Xu, Bao Zhang, Stephen Lin, and Rabab Kreidieh Ward. 2015. Object-based multiple foreground video co-segmentation via multi-state selection graph. *IEEE TIP* (2015).
- [9] Qibin Hou, Ming-Ming Cheng, Xiao-Wei Hu, Ali Borji, Zhuowen Tu, and Philip Torr. 2017. Deeply supervised salient object detection with short connections. In *CVPR*.
- [10] Yangqing Jia, Evan Shelhamer, Jeff Donahue, Sergey Karayev, Jonathan Long, Ross Girshick, Sergio Guadarrama, and Trevor Darrell. 2014. Caffe: Convolutional architecture for fast feature embedding. In *ACM Multimedia*.
- [11] Huaizu Jiang, Jingdong Wang, Zejian Yuan, Tie Liu, Nanning Zheng, and Shipeng Li. 2011. Automatic salient object segmentation based on context and shape prior. In *Bmvc*.
- [12] Huaizu Jiang, Jingdong Wang, Zejian Yuan, Yang Wu, Nanning Zheng, and Shipeng Li. 2013. Salient Object Detection: A Discriminative Regional Feature Integration Approach. In *CVPR*.
- [13] Peng Jiang, Nuno Vasconcelos, and Jingliang Peng. 2015. Generic Promotion of Diffusion-Based Salient Object Detection. In *ICCV*.
- [14] Jiwhan Kim, Dongyoon Han, Yu-Wing Tai, and Junmo Kim. 2014. Salient region detection via high-dimensional color transform. In *CVPR*.
- [15] Gayoung Lee, Yu-Wing Tai, and Junmo Kim. 2016. Deep saliency with encoded low level distance map and high level features. In *CVPR*.
- [16] Fuxin Li, Taeyoung Kim, Ahmad Humayun, David Tsai, and James M Rehg. 2013. Video segmentation by tracking many figure-ground segments. In *ICCV*.
- [17] Guanbin Li and Yizhou Yu. 2016. Deep contrast learning for salient object detection. In *CVPR*.
- [18] Jia Li, Changqun Xia, and Xiaowu Chen. 2018. A Benchmark Dataset and Saliency-guided Stacked Autoencoders for Video-based Salient Object Detection. *IEEE TIP* (2018).
- [19] Jia Li, Anlin Zheng, Xiaowu Chen, and Bin Zhou. 2017. Primary Video Object Segmentation via Complementary CNNs and Neighborhood Reversible Flow. In *ICCV*.
- [20] Xiaohui Li, Huchuan Lu, Lihe Zhang, Xiang Ruan, and Ming-Hsuan Yang. 2013. Saliency detection via dense and sparse reconstruction. In *ICCV*.
- [21] Nian Liu and Junwei Han. 2016. Dhsnet: Deep hierarchical saliency network for salient object detection. In *CVPR*.
- [22] T. Liu, Z. Yuan, J. Sun, J. Wang, N. Zheng, X. Tang, and H. Y. Shum. 2011. Learning to Detect a Salient Object. *IEEE TPAMI* (2011).
- [23] Francesco Mancini, Marco Dubbini, Mario Gattelli, Francesco Stecchi, Stefano Fabbri, and Giovanni Gabbianelli. 2013. Using Unmanned Aerial Vehicles (UAV) for High-Resolution Reconstruction of Topography: The Structure from Motion Approach on Coastal Environments. *Remote Sensing* (2013).

- [24] Ran Margolin, Lihl Zelnik-Manor, and Ayellet Tal. 2014. How to evaluate foreground maps?. In *CVPR*.
- [25] Anestis Papazoglou and Vittorio Ferrari. 2013. Fast object segmentation in unconstrained video. In *ICCV*.
- [26] Houwen Peng, Bing Li, Haibin Ling, Weiming Hu, Weihua Xiong, and Stephen J Maybank. 2017. Salient object detection via structured matrix decomposition. *IEEE TPAMI* (2017).
- [27] Federico Perazzi, Jordi Pont-Tuset, Brian McWilliams, Luc Van Gool, Markus Gross, and Alexander Sorkine-Hornung. 2016. A benchmark dataset and evaluation methodology for video object segmentation. In *CVPR*.
- [28] Yao Qin, Huchuan Lu, Yiqun Xu, and He Wang. 2015. Saliency detection via cellular automata. In *CVPR*.
- [29] Esa Rahtu, Juho Kannala, Mikko Salo, and Janne Heikkil. 2010. Segmenting Salient Objects from Images and Videos. In *ECCV*.
- [30] Bryan C. Russell, Antonio Torralba, Kevin P. Murphy, and William T. Freeman. 2008. LabelMe: A Database and Web-Based Tool for Image Annotation. *IJCV* (2008).
- [31] Tianmin Shu, D. Xie, B. Rothrock, S. Todorovic, and S. C. Zhu. 2015. Joint inference of groups, events and human roles in aerial videos. In *CVPR*.
- [32] Karen Simonyan and Andrew Zisserman. 2014. Very deep convolutional networks for large-scale image recognition. *arXiv preprint arXiv:1409.1556* (2014).
- [33] D Tsai, M Flagg, and J Rehg. 2010. Motion coherent tracking with multi-label mrf optimization, algorithms. In *BMVC*.
- [34] Wei-Chih Tu, Shengfeng He, Qingxiang Yang, and Shao-Yi Chien. 2016. Real-Time Salient Object Detection With a Minimum Spanning Tree. In *CVPR*.
- [35] Lijun Wang, Huchuan Lu, Xiang Ruan, and Ming-Hsuan Yang. 2015. Deep networks for saliency detection via local estimation and global search. In *CVPR*.
- [36] Linzhao Wang, Lijun Wang, Huchuan Lu, Pingping Zhang, and Xiang Ruan. 2016. Saliency detection with recurrent fully convolutional networks. In *ECCV*.
- [37] Wenguan Wang, Jianbing Shen, and Fatih Porikli. 2015. Saliency-Aware Geodesic Video Object Segmentation. In *CVPR*.
- [38] Wenguan Wang, Jianbing Shen, and Ling Shao. 2015. Consistent video saliency using local gradient flow optimization and global refinement. *IEEE TIP* (2015).
- [39] Changqun Xia, Jia Li, Xiaowu Chen, Anlin Zheng, and Yu Zhang. 2017. What Is and What Is Not a Salient Object? Learning Salient Object Detector by Ensembling Linear Exemplar Regressors. In *CVPR*.
- [40] Qiong Yan, Li Xu, Jianping Shi, and Jiaya Jia. 2013. Hierarchical saliency detection. In *CVPR*.
- [41] Chuan Yang, Lihe Zhang, Huchuan Lu, Xiang Ruan, and Ming-Hsuan Yang. 2013. Saliency Detection via Graph-Based Manifold Ranking. In *CVPR*.
- [42] Dong Zhang, Omar Javed, and Mubarak Shah. 2014. Video object co-segmentation by regulated maximum weight cliques. In *ECCV*.
- [43] Jianming Zhang, Stan Sclaroff, Zhe Lin, Xiaohui Shen, Brian Price, and Radomir Mech. 2015. Minimum barrier salient object detection at 80 fps. In *ICCV*.
- [44] J. Zhang, Y. Wu, W. Liu, and X. Chen. 2010. Novel Approach to Position and Orientation Estimation in Vision-Based UAV Navigation. *IEEE Trans. Aerospace Electron. Systems* (2010).
- [45] Rui Zhao, Wanli Ouyang, Hongsheng Li, and Xiaogang Wang. 2015. Saliency detection by multi-context deep learning. In *CVPR*.
- [46] Wangjiang Zhu, Shuang Liang, Yichen Wei, and Jian Sun. 2014. Saliency optimization from robust background detection. In *CVPR*.